

# Impact of Nonlocal Coulomb Repulsion on Superconductivity and Density-Wave Orders in Bilayer Nickelates

Jun Zhan,<sup>1,2</sup> Congcong Le,<sup>3</sup> Xianxin Wu,<sup>4,\*</sup> and Jiangping Hu<sup>1,5,6,†</sup>

<sup>1</sup>Beijing National Laboratory for Condensed Matter Physics and Institute of Physics, Chinese Academy of Sciences, Beijing 100190, China

<sup>2</sup>School of Physical Sciences, University of Chinese Academy of Sciences, Beijing 100190, China

<sup>3</sup>RIKEN Interdisciplinary Theoretical and Mathematical Sciences (iTHEMS), Wako, Saitama 351-0198, Japan

<sup>4</sup>CAS Key Laboratory of Theoretical Physics, Institute of Theoretical Physics, Chinese Academy of Sciences, Beijing 100190, China

<sup>5</sup>Kavli Institute for Theoretical Sciences, University of Chinese Academy of Sciences, Beijing 100190, China

<sup>6</sup>New Cornerstone Science Laboratory, Beijing 100190, China

The recent discovery of high-temperature superconductivity in pressurized bilayer nickelate  $\text{La}_3\text{Ni}_2\text{O}_7$  and its thin films has sparked significant interest in understanding their pairing mechanism and correlated states. While previous theoretical studies have mainly focused on onsite Coulomb interactions, the role of nonlocal Coulomb repulsion has been neglected, leaving its effect unexplored and elusive. In this work, we comprehensively explore the effect of nonlocal Coulomb repulsion on both superconductivity and density-wave orders in the presence of onsite interactions by performing functional renormalization group calculations. We find that interlayer repulsion suppresses the interlayer intra-orbital  $s_{\pm}$ -wave pairing and spin-density-wave order, while driving a transition to an interlayer inter-orbital  $d_{x^2-y^2}$ -wave pairing and a mirror-symmetry breaking charge order. This transition occurs across a wide range of charge doping and is independent of the presence of the  $\gamma$  pocket around M point. Remarkably, the critical scale of the  $d_{x^2-y^2}$ -wave superconductivity is significantly lower than that of the  $s_{\pm}$ -wave superconductivity, suggesting that the former pairing is unlikely to account for the observed high- $T_c$  superconductivity. Additionally, the intralayer nearest-neighbor repulsion promotes an in-plane charge density wave order with a vector of  $(\pi, \pi)$ . Our findings highlight profound impact of nonlocal Coulomb repulsion and the robustness of interlayer pairing associated with the bilayer structure and multi-orbital nature, advancing the understanding of the complex correlation effects within bilayer nickelates.

## I. INTRODUCTION

Exploring high-temperature superconductivity and revealing pairing mechanism are among the most challenging problems in condensed matter physics [1]. High- $T_c$  cuprates and iron based superconductors (IBS) have long served as two paradigmatic systems with distinctive characteristics: cuprates feature  $d^9$  configuration in the octahedral complex with a single active  $d_{x^2-y^2}$  orbital [2], while IBS feature  $d^6$  in the tetrahedral complex with three active  $t_{2g}$  orbitals [3]. Surprisingly, a new type of bilayer nickelate  $\text{La}_3\text{Ni}_2\text{O}_7$  (LNO) in the Ruddlesden-Popper phase has been recently discovered to exhibit superconductivity under pressure with an extraordinary  $T_c$  of nearly 80 K [4], introducing a third high- $T_c$  family. Different from its predecessors, LNO hosts  $\text{Ni}^{2.5+}$  with a  $d^{7.5}$  configuration, where both  $d_{x^2-y^2}$  and  $d_{z^2}$  orbitals contribute to the low-energy physics, enabled by the presence of apical oxygens between layers [5–11]. Under ambient conditions, LNO is in the *Amam* phase and features density wave orders at low pressures [12–20]. With increasing pressure, superconductivity suddenly emerges following a structural transition to the *Fmmm*/*I4mmm*, accompanied by reduced layer separation and stretching the apical Ni-O-Ni bond angle from  $168^\circ$  toward  $180^\circ$ . Additionally, trilayer nickelate  $\text{La}_4\text{Ni}_3\text{O}_{10}$  also exhibits superconductivity, with a lower  $T_c$  of 20-30 K, when its ambient density wave order is suppressed under pressure [21–25]. Strikingly, superconductivity with a  $T_c$  ex-

ceeding 40 K has been achieved in compressively strained LNO thin films on the substrate  $\text{SrLaAlO}_4$  at ambient pressure [26, 27]. So far, the crucial ingredients for superconductivity remain unclear, but recent experiments reveal an intimate relationship between superconductivity and spin density wave (SDW) order [28], implying an important role of magnetic fluctuations.

Pairing mechanism of LNO has been under intensive theoretical study since the discovery of superconductivity, and a consensus is yet to be reached [8, 9, 29–49]. Theoretical calculations suggest that the pressure-driven Lifshitz transition, i.e. the  $d_{z^2}$  interlayer bonding state crosses the Fermi level to form a hole pocket, is crucial for bulk superconductivity under pressure [4]. From the perspective of weak to intermediate coupling, spin fluctuations are believed to promote an  $s_{\pm}$ -wave pairing following the Lifshitz transition [8, 9, 29, 33], where the interlayer pairing in the  $d_{z^2}$  orbital is dominant. In the strong-coupling regime, the itinerant  $d_{x^2-y^2}$  orbital acquiring an effective exchange coupling through Hund's coupling [30, 31, 34] or inter-orbital hybridization between  $d_{x^2-y^2}$  and  $d_{z^2}$  orbitals [35] plays an important role in driving interlayer pairing of the  $d_{x^2-y^2}$  orbital. While these studies have focused primarily on on-site Coulomb repulsion, the nonlocal Coulomb repulsion has been completely neglected. However, this interaction can be particularly relevant in LNO for several reasons: (1) the interatomic distance is reduced in under pressure, enhancing nonlocal repulsion; (2) the two active orbitals,  $d_{x^2-y^2}$  and  $d_{z^2}$ , exhibit strong hybridization with in-plane and apical oxygen, leading to extended Wannier functions; (3) the screening effect is weak in the direction perpendicular to the  $\text{NiO}_2$  planes, promoting interlayer repulsion. Indeed, constrained random

\*Electronic address: xxwu@itp.ac.cn

†Electronic address: jphu@iphy.ac.cn

phase approximation calculations reveal that nearest-neighbor Coulomb repulsion is sizable and can not be neglected [50]. The presence of nonlocal Coulomb repulsion, particularly the interlayer interaction, can profoundly affect on the interlayer pairing and the instability of charge/spin density wave within the bilayer structure. Consequently, it is essential to clarify the impact of nonlocal interaction on the correlated states in LNO.

In this work, we comprehensively investigate the effect of nonlocal Coulomb repulsion on both superconductivity and density-wave orders in the presence of onsite interactions by employing FRG calculations for LNO. We consider both interlayer and intralayer nonlocal repulsion for the cases with and without  $d_{z^2}$  bonding  $\gamma$  hole pocket. In both fermiology, the interlayer repulsion suppresses the interlayer intra-orbital  $s_{\pm}$  pairing, and drives a transition to an interlayer inter-orbital  $d_{x^2-y^2}$  pairing and a charge order that breaks the mirror symmetry of the bilayer. In the presence of  $\gamma$  pocket, interlayer repulsion drives a transition from  $s_{\pm}$ -wave superconductivity to metal and then to  $d_{x^2-y^2}$ -wave superconductivity with moderate Hund's coupling. In the absence of  $\gamma$  pocket, in contrast, it drives a direct transition from either  $s_{\pm}$ -wave superconductivity or SDW to  $d_{x^2-y^2}$ -wave superconductivity. Such transition occurs over a large range of charge doping. Remarkably, the critical scale of the  $d_{x^2-y^2}$ -wave superconductivity is typically much lower than that of the corresponding  $s_{\pm}$ -wave superconductivity, suggesting that this  $d_{x^2-y^2}$  pairing is unlikely to be responsible for observed high- $T_c$  superconductivity. Additionally, the intralayer nearest-neighbor repulsion promotes an in-plane CDW order with a vector of  $(\pi, \pi)$  by suppressing  $s_{\pm}$ -wave superconductivity and SDW order. These results are relevant to LNO under both ambient and high-pressure conditions, as well as to thin films with in-plane strains. Finally, we discuss potential experimental implications of our findings.

## II. MODEL

We start with the effective model for LNO. The low-energy electronic structures of bilayer nickelates LNO are dominated by Ni  $d_{x^2-y^2}$  and  $d_{z^2}$  orbitals according to theoretical calculations and experimental measurements [5–11]. Therefore, the low-energy physics can be described by a two-orbital tight-binding (TB) Hamiltonian [5–9], which reads,

$$\mathcal{H}_0 = \sum_{ij, \alpha\beta, \sigma} t_{\alpha\beta}^{ij} c_{i\alpha\sigma}^\dagger c_{j\beta\sigma} - \mu \sum_{i\alpha\sigma} c_{i\alpha\sigma}^\dagger c_{j\alpha\sigma}. \quad (1)$$

Here  $i, j = (m, l)$  labels the in-plane lattice site ( $m$ ) and layer index ( $l = t, b$ ),  $\sigma$  labels spin, and  $\alpha, \beta = x, z$  labels the Ni orbitals with  $x$  denoting the  $d_{x^2-y^2}$  and  $z$  the  $d_{z^2}$  orbital.  $\mu$  is the chemical potential and the adopted hopping parameters are provided in Ref. [9]. At high pressure, it is believed that the  $d_{z^2}$  bonding state crosses the Fermi level and plays an important role in promoting superconductivity [4]. The corresponding band structure is shown in Fig.1(a), where  $d_{x^2-y^2}$  and  $d_{z^2}$  orbitals are represented by red and blue colors, respectively. The Fermi surfaces (FS) at the average filling  $n = 3$  per

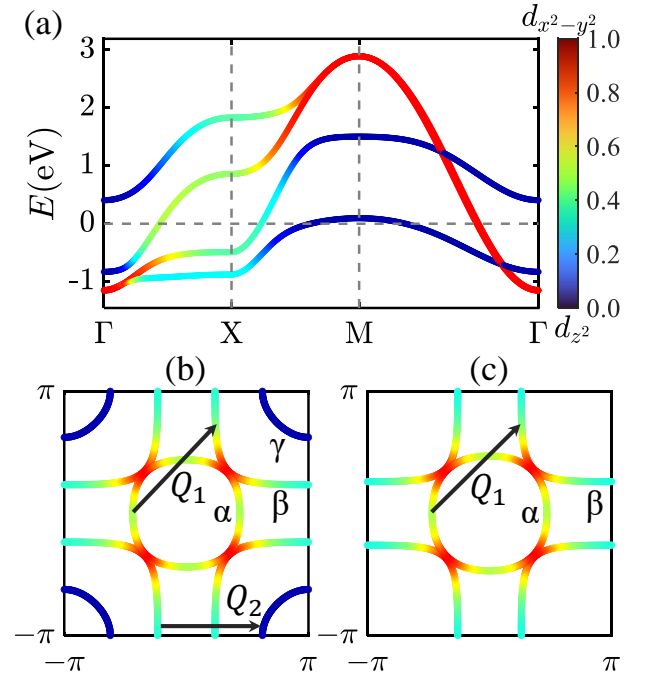


FIG. 1: (color online) (a) Orbital-resolved band structure with orbital contributions is represented by colors. FS from the tight-binding model at filling  $n = 3$  (b) and  $n=3.33$  (c) with corresponding FS nesting vector marked by  $\mathbf{Q}_{1,2}$ .

site (1.5 per Ni atom) is illustrated in Fig.1(b), which contains three pockets: the  $\alpha$  electron pocket arises from the interlayer bonding state of  $d_{x^2-y^2}$  and  $d_{z^2}$  orbital and the hole-like  $\beta$  and  $\gamma$  pockets originate mainly from the interlayer anti-bonding state of  $d_{x^2-y^2}$  and bonding state of  $d_{z^2}$  orbital, respectively. The antibonding  $\beta$  pocket shows a good nesting with bonding  $\alpha$  and  $\gamma$  pocket at wave vector  $\mathbf{Q}_1$  and  $\mathbf{Q}_2$ , respectively. These nesting contribute to antiferromagnetic fluctuations at  $\mathbf{Q}_{1,2}$  with interlayer antiferromagnetic coupling [51]. To study the correlated states with the same fermiology at ambient pressure, where  $\alpha$  and  $\beta$  pockets are present, we adjust the Fermi level to introduce 1/3 electron doping and the resulting FS are shown in (Fig.1(c)). The  $\alpha$  and  $\beta$  pockets still show a good nesting with wave vector  $\mathbf{Q}_1$ .

For the interacting part of Hamiltonian, we consider the general multi-orbital on-site Hubbard interactions and nearest-neighbor Coulomb repulsion,

$$\begin{aligned} \mathcal{H}_{\text{EI}} = & \sum_{i\alpha} U n_{i\alpha\uparrow} n_{i\alpha\downarrow} + \sum_{i, \alpha \neq \beta} J_P c_{i\alpha\uparrow}^\dagger c_{i\alpha\downarrow}^\dagger c_{i\beta\downarrow} c_{i\beta\uparrow} \\ & + \sum_{i, \alpha < \beta, \sigma\sigma'} (U' n_{i\alpha\sigma} n_{i\beta\sigma'} + J_H c_{i\alpha\sigma}^\dagger c_{i\beta\sigma} c_{i\beta\sigma'}^\dagger c_{i\alpha\sigma'}) \\ & + \sum_{\langle ij \rangle \sigma\sigma'} V_{ij}^{\alpha\beta} n_{i\alpha\sigma} n_{j\beta\sigma'}. \end{aligned} \quad (2)$$

Here  $U/U'$  are the intra/inter-orbital Hubbard repulsion,  $J_H$  is the Hund's coupling,  $J_P$  is the pair-hopping interaction,  $V_{ij=\perp/\parallel}^{\alpha\beta}$  denotes interlayer/intralayer repulsion between  $\alpha$

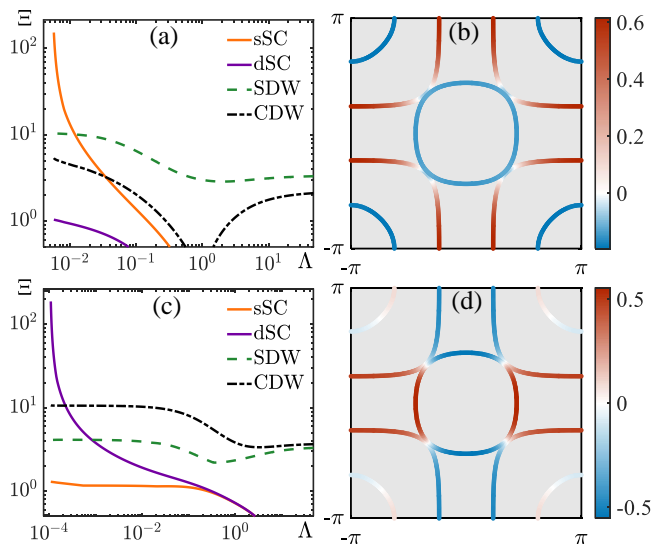


FIG. 2: (color online) FRG flow and leading superconducting gap function on FS with  $J = 0.3$  eV, out-of-plane repulsion  $V_{\perp} = 0$  (a,b) and  $V_{\perp} = 1.4$  eV (c,d) at filling  $n = 3$ .  $U = 3$  eV is adopted in the calculations unless otherwise specified.

and  $\beta$  orbitals. These nonlocal Coulomb repulsions, derived from delocalized Wannier functions and weak screening effect, are the focus of our study. In the following, the standard Kanamori relations  $U = U' + 2J_H$  and  $J_H = J_P$  [52] are adopted in this work. Regarding nonlocal intra-orbital repulsion, we take approximate relations  $V_{\perp}^{zz} = 2V_{\perp}^{xx} = V_{\perp}$  for the interlayer terms and  $V_{\parallel}^{xx} = 2V_{\parallel}^{zz} = V_{\parallel}$  for the intralayer term [50], due to spatial orientation of these two orbitals. But our conclusions are robust against these relations.

The correlated states have been studied from both weak-coupling and strong-coupling perspective, yet a consensus remains elusive. Recent experiments show that the magnetic order exhibits small magnetic local moments and itinerant characteristics [14, 16, 17, 20], in analogous to IBS. Consequently, we adopt the functional renormalization group (FRG) approach, which treats all particle-hole and particle-particle channels on equal footing, and it provides a nuanced depiction of correlated states spanning from weak to intermediate coupling regimes [53–55]. We implement FRG in the truncated unity or singular mode formalism [56, 57] and use a hard Matsubara frequency cutoff as regulator with details provided in Appendix A. Compared to previous studies, our work explores the impacts of interlayer/intralayer nonlocal repulsion on correlated states within the bilayer two-orbit model using the FRG approach.

### III. RESULTS

#### A. Effect of interlayer repulsion with $\gamma$ pocket

We first study the effect of interlayer repulsion for the case with  $\gamma$  pocket. With only on-site interactions, the typical FRG

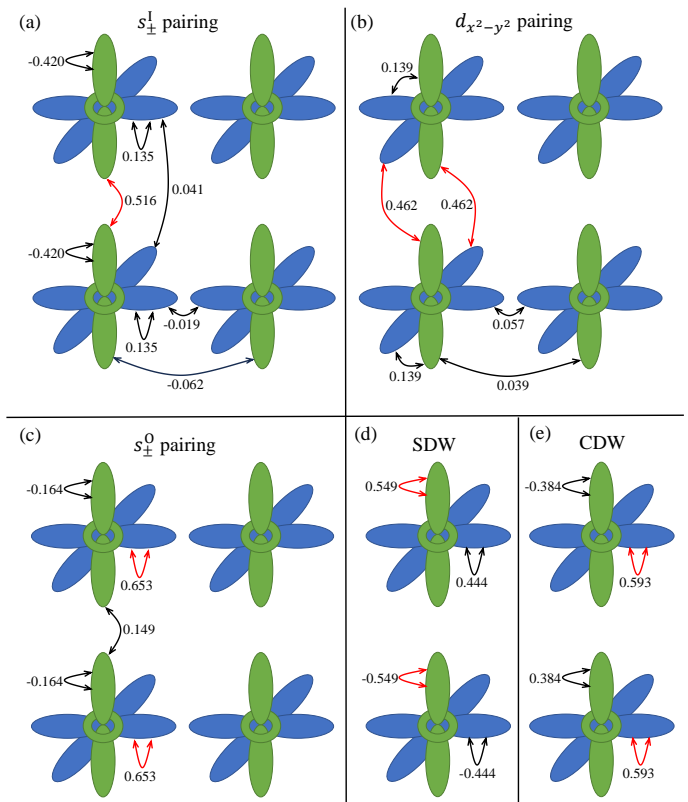


FIG. 3: (color online) Typical real space order parameter pattern of (a) interlayer pairing dominated  $s_{\pm}^I$  superconductivity at  $J = 0.3$  eV,  $V_{\perp} = 0$ ; (b)  $d_{x^2-y^2}$  pairing at  $J = 0.3$  eV,  $V_{\perp} = 1.4$  eV; (c) intralayer pairing dominated  $s_{\pm}^O$  superconductivity at  $J = 0.3$  eV,  $V_{\perp} = 1.6$  eV; (d) SDW at  $J = 0.6$  eV,  $V_{\perp} = 0$ ; (e) charge order at  $J = 0.2$  eV,  $V_{\perp} = 1.4$  eV and  $U = 3$  eV,  $n = 3$ . Not all significant components of superconductivity are explicitly shown. The other components are derived through lattice symmetry by applying the transformation properties of irreducible representations. Red line indicate the dominant pairing components.

flow of leading eigenvalues  $\Xi$  in different channels with representative parameters  $U = 3$  eV and  $J = 0.1U$  is illustrated in Fig. 2(a). The dominant instability is  $s_{\pm}$ -wave superconductivity, while SDW, CDW and  $d_{x^2-y^2}$ -wave superconductivity are subdominant. The  $s_{\pm}$  superconducting gap exhibits a sign change between the bonding  $\alpha, \gamma$  and antibonding  $\beta$  pockets, as depicted in Fig. 2(b). This pairing state aligns with the scenario of spin fluctuation-mediated pairing, where pockets connected by wave vectors  $\mathbf{Q}_1$  and  $\mathbf{Q}_2$  display sign-reversed gaps. In addition, the pairing dominantly involves interlayer pairing in the  $d_{z^2}$  orbital, labeled as  $s_{\pm}^I$ , according to the real-space pairing components shown in Fig. 3(a). As the pairing gap on the bonding (anti-bonding) band is the sum (difference) of onsite and interlayer pairings, this interlayer-pairing dominated  $s_{\pm}^I$  pairing naturally leads to sign-opposite superconducting gaps on bonding and antibonding pockets.

The further inclusion of interlayer intraorbital repulsion will suppress the interlayer pairing and promote interlayer charge fluctuations. According to our calculations,  $V_{\perp}$  will gradually suppress the  $s_{\pm}^I$ -wave pairing and transition into

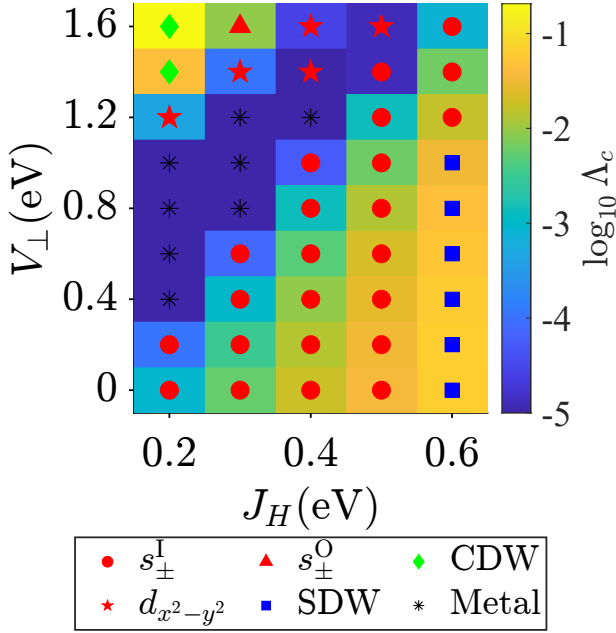


FIG. 4: (color online) Out-of-plane  $V_{\perp}$ -Hund coupling phase diagram for  $U = 3$  eV and  $V_{\perp}^{zz} = 2V_{\perp}^{xx} = V_{\perp}$  denote at filling  $n = 3$ , with the color bar indicate critical scales  $\Lambda_c$  at which the corresponding FRG flows diverges. Here,  $s_{\pm}^I$  and  $s_{\pm}^O$  denote interlayer-dominated and on-site-dominated  $s_{\pm}$ -wave superconductivity respectively. In the region marked by black star, the RG flow exhibits no divergence above the scale of  $10^{-5}$  so we label it as Metal.

a metallic phase in which FRG flow exhibits no divergence above the scale of  $10^{-5}$ . With further increasing  $V_{\perp}$ , another  $d_{x^2-y^2}$ -wave pairing emerges. Fig. 2(c) shows a typical flow with an intermediate  $V_{\perp}$ , where  $d_{x^2-y^2}$  superconductivity diverges at a very low critical scale. It is apparent that SDW fluctuation gets suppressed and CDW fluctuation is promoted, compared with the case of onsite interactions. As shown in Fig. 2(d), the  $d_{x^2-y^2}$ -wave gap function exhibits nodes along  $\Gamma - M$  direction and nearly vanishing gap on the  $\gamma$  pocket as well. Moreover, the gaps on the  $\alpha$  and  $\beta$  pockets are sign-reversed. To identify the origin, we calculate the real-space pairing components and plot them in Fig. 3(b). Remarkably, we observe that the in-plane pairing components are rather weak and the dominant pairing occurs within the interlayer inter-orbital channel. This is in contrast to the  $d_{x^2-y^2}$  pairing in the single-orbital Hubbard model, where pairing occurs mainly between the nearest-neighbor sites. The inter-orbital pairing results in maximum gaps on  $\alpha, \beta$  pockets with mixed orbital characters and a nearly vanishing gap on the  $\gamma$  pocket due to its dominant  $d_{z^2}$  weight as shown in Fig. 1(b). The interlayer pairing will also induce sign-reversed gaps on the bonding ( $\alpha$ ) and antibonding ( $\beta$ ) pockets, dictated by the FS nesting at  $\mathbf{Q}_1$ . These explain the gap features in the momentum space. The interlayer inter-orbital pairing, which is uniquely associated with the bilayer structure, becomes leading as the interlayer intra-orbital pairing is suppressed and charge fluctuation gets enhanced by the interlayer Coulomb repulsion.

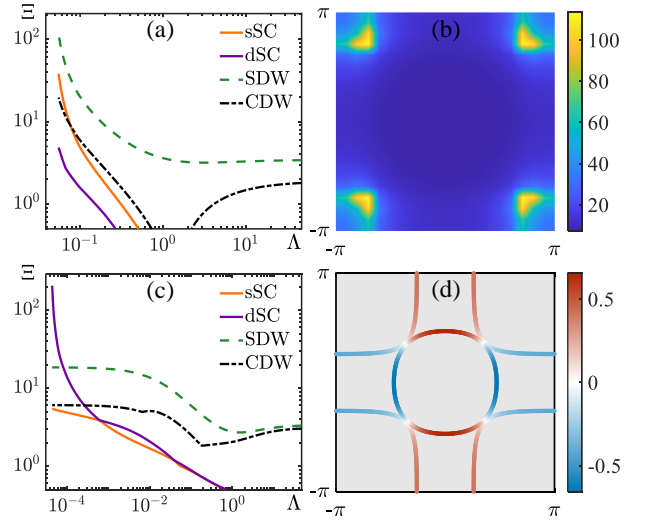


FIG. 5: (color online) SDW and  $d_{x^2-y^2}$  pairing instability at filling  $n = 3.33$ . (a,b)FRG flow and  $\mathbf{q}$  dependence of leading effective interaction in SDW channels at  $U = 3$  eV,  $J = 0.4$  eV,  $V_{\perp} = 0$ . (c,d) FRG flow and leading superconducting gap functions on FS at  $U = 3$  eV,  $J = 0.4$  eV and  $V_{\perp} = 1.4$  eV.

Furthermore, we present a representative phase diagram as a function of Hund's coupling strength  $J_H$  and out-of-plane repulsion  $V_{\perp}$  in Fig. 4. The  $s_{\pm}^I$  superconductivity dominates in the weak  $V_{\perp}$  regime. With increasing  $V_{\perp}$ ,  $s_{\pm}^I$  pairing gets suppressed to a metallic phase and further gives way to  $d_{x^2-y^2}$  pairing for intermediate  $V_{\perp}$ . This transition occurs in a wide  $J_H$  regime. There is also a competing spin-triplet  $p$ -wave pairing state near the phase boundary of between  $s_{\pm}$ -wave pairing or metal and  $d_{x^2-y^2}$ -wave pairing. This triplet pairing stems from strong ferromagnetic spin fluctuations associated with the flat  $d_{z^2}$  band around the M point. In the regime of weak Hund's coupling  $J_H$ , a charge order and  $s_{\pm}^O$ -wave superconducting can emerge as the leading instabilities. This charge order does not break the translational symmetry but the out-of-plane mirror reflection, as shown in Fig. 3(e). The  $s_{\pm}^O$ -wave pairing is characterized by dominant onsite pairing within the  $d_{x^2-y^2}$  orbital, as shown in Fig. 3(c), and arises due to strong charge fluctuations. Repulsive pair hopping interaction leads to sign-reversed gap on  $d_{z^2}$  and  $d_{x^2-y^2}$  orbitals. This results in  $s_{\pm}^O$  pairing exhibiting sign-changed gap between  $d_{z^2}$ -dominated  $\gamma$  pocket and  $d_{x^2-y^2}$ -dominated  $\alpha/\beta$  pockets. In the regime of strong Hund's coupling  $J_H$ , there is a direct transition from an SDW state to  $s_{\pm}^I$ -wave superconducting with increasing interlayer repulsion, originating from the suppressed interlayer antiferromagnetic coupling.

## B. Effect of interlayer repulsion without $\gamma$ pocket

The  $\gamma$  pocket is crucial to stabilize the  $s_{\pm}^I$ -wave pairing [51]. In this section, we study the impact of interlayer repulsion on correlated state in the absence of the  $\gamma$  pocket. To achieve it, we adjust the Fermi level to lie above the top of the

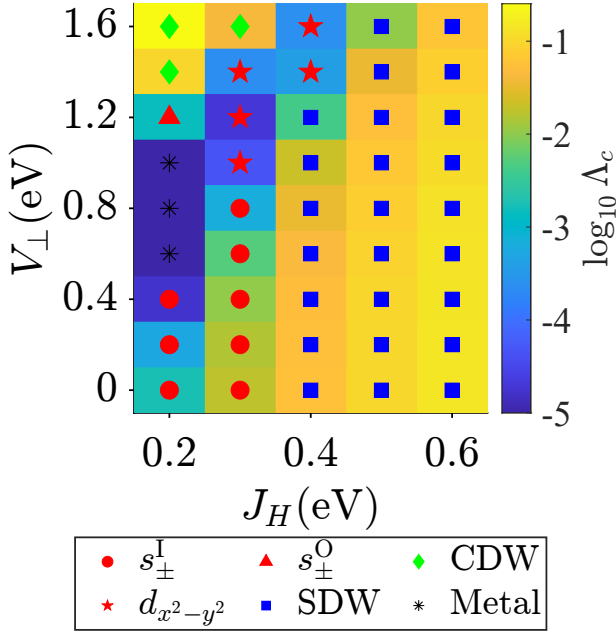


FIG. 6: (color online) Out-of-plane  $V_{\perp}$ - Hund's coupling phase diagram for  $U = 3$  eV and  $V_{\perp}^{zz} = 2V_{\perp}^{xx} = V_{\perp}$  at filling  $n=3.33$ .

$d_{z^2}$  bonding band and the resulting Fermi surfaces are shown in Fig. 1(c), where  $\alpha, \beta$  pockets are almost identical to those in Fig. 1(b). In this case, typical FRG flow with only onsite interactions is shown in Fig. 5(a), where SDW fluctuations get significantly enhanced. The system develops an SDW instability with a wavevector of  $\mathbf{Q}_1$  at a relatively high critical scale. The real-space pattern of this SDW is displayed in Fig. 3(d), where the interlayer coupling is antiferromagnetic. With further including the interlayer repulsion, the SDW order is suppressed. When  $V_{\perp}$  is above a critical value, the leading instability transitions to the  $d_{x^2-y^2}$ -wave superconductivity directly from SDW. Fig. 5(c) illustrates the FRG flow for a strong  $V_{\perp}$ , where charge fluctuations remain consistently weaker than magnetic fluctuations. The critical scale of  $d_{x^2-y^2}$ -wave superconductivity is quite low and the gap function is shown in Fig. 5(d), both of which are similar to the case with  $\gamma$  pocket. In the regime of weak Hund's coupling, as shown in Fig. 6,  $s_{\pm}^I$ -wave superconductivity emerges with only onsite interactions and it transitions to  $d_{x^2-y^2}$ -wave,  $s_{\pm}^O$ -wave superconductivity and out-of-plane charge order as  $V_{\perp}$  increases. As the inter-orbital pairing vanishes on the  $\gamma$  pocket, its absence has negligible effect on  $d_{x^2-y^2}$ -wave pairing. With strong Hund's coupling, the SDW order dominates and a large  $V_{\perp}$  is needed to fully suppress it.

### C. Effects of doping and intralayer repulsion

We further systematically study the effect of  $V_{\perp}$  as a function of doping. The resulting phase diagram of out-of-plane repulsion versus doping with typical onsite interaction  $U = 3$  eV and  $J = 0.1U$  is shown in Fig. 7. At low  $V_{\perp}$ , electron doping enhances the transition temperature of the  $s_{\pm}^I$ -wave pair-

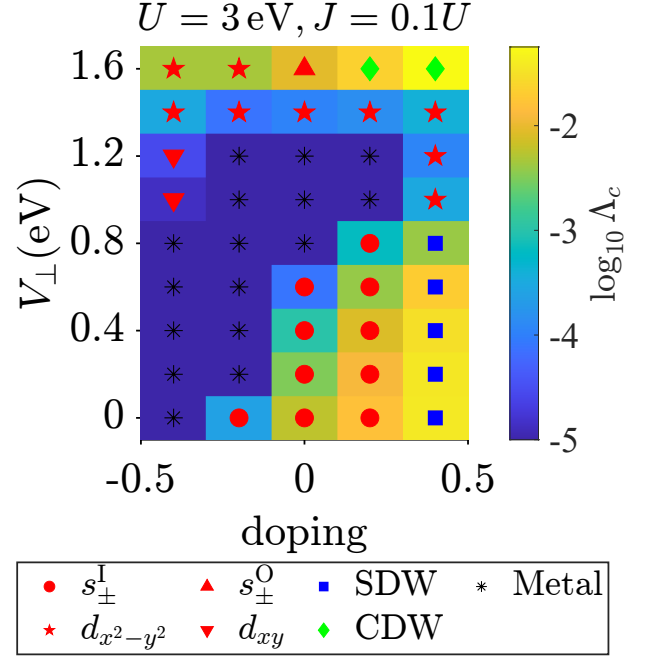


FIG. 7: (color online) Out-of-plane  $V_{\perp}$ - doping phase diagram for  $U = 3$  eV,  $J = 0.1U$ ,  $V_{\perp}^{zz} = 2V_{\perp}^{xx} = V_{\perp}$ .

ing owing to the enhanced density of states on the  $\gamma$  pocket. While excessive electron doping drives the system into the SDW state due to the elimination of the  $\gamma$  pocket. At electron doping side, the interlayer  $s_{\pm}$  pairing is relatively stable at low  $V_{\perp}$  regime. However, superconductivity is destroyed with heavy hole doping. The transition from  $s_{\pm}^I$ -wave pairing to  $d_{x^2-y^2}$ -wave pairing with increasing  $V_{\perp}$  exists in a large range of charge doping.

As a comparison, we also investigate the effect of intralayer nearest-neighbor repulsion on correlated state. As all relevant pairings occur in the interlayer channel, the intralayer does not directly suppress pairing but rather weakens it indirectly through diminishing magnetic fluctuations. Our FRG calculations show that the intralayer repulsion suppresses both superconductivity and SDW and drive the system into a CDW order with  $\mathbf{Q} = (\pi, \pi)$ , as depicted in Fig. 8. This occurs both with and without  $\gamma$  pocket. The critical intralayer repulsion is around 0.5 eV for  $U=3$  eV and is independent of the presence of the  $\gamma$  pocket, which is much smaller than the critical value required to drive a phase transition in the case of interlayer repulsion. The CDW exhibits an in-plane charge density modulation with  $\mathbf{Q} = (\pi, \pi)$  to minimize the intralayer repulsion.

## IV. DISCUSSIONS AND CONCLUSIONS

Our findings reveal the profound influence of nonlocal Coulomb repulsion on the superconducting and density-wave instabilities and intrinsic characteristics of the bilayer nickelate LNO. Conventionally, we would expect that the interlayer repulsion suppresses the interlayer pairing and pushes the

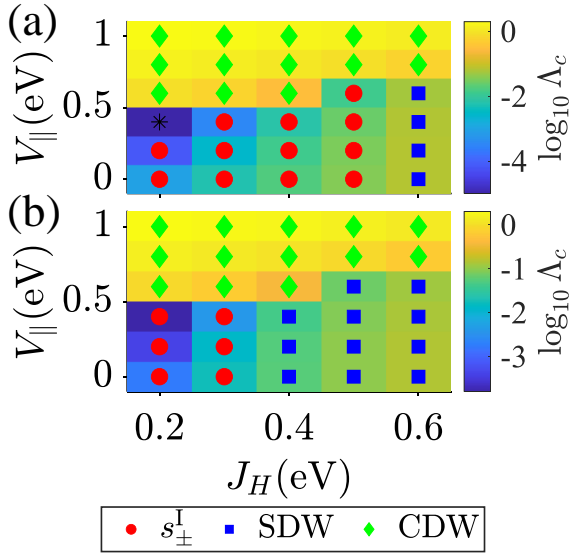


FIG. 8: (color online) In-plane repulsion  $V_{\parallel}$ -Hund's coupling  $J_H$  phase diagram for  $U = 3$  eV,  $V_{\parallel}^{xx} = 2V_{\parallel}^{zz} = V_{\parallel}$  at filling  $n = 3$  (a) and  $n = 3.33$  (b).

pairing into the in-plane nearest-neighbor channel. However, owing to the multi-orbital nature an interlayer inter-orbital pairing emerges to avoid strong interlayer intra-orbital repulsion. Additionally, even when both interlayer intra-orbital and inter-orbital repulsion are included, the  $s_{\pm}^I$ -wave pairing can be enhanced and its transition to the  $d_{x^2-y^2}$ -wave pairing persists, albeit at larger values of  $V_{\perp}$  (see Appendix B). The prominence of interlayer pairing under these interacting setting suggest its robustness within the bilayer structure, in contrast to cuprates and IBS. According to our calculations, the transition temperature of  $d_{x^2-y^2}$ -wave superconductivity is usually much lower than that of  $s_{\pm}^I$ -wave superconductivity, as the interlayer repulsion significantly suppresses interlayer magnetic couplings. It implies that  $d_{x^2-y^2}$ -wave pairing may not be responsible for the observed high- $T_c$  superconductivity in experiments. Strong interlayer and intralayer repulsion can drive charge orders, breaking mirror reflection and translational symmetry, respectively. These orders can be entangled with SDW orders, generating the complex spin-charge stripe order observed in experiments [16, 17, 20]. The nonlocal Coulomb repulsion can further have an intricate interplay with interlayer electron-phonon coupling, influencing both superconductivity and density-wave orders [32].

In conclusion, we have systematically explored the effect of nonlocal Coulomb repulsion on both superconductivity and density-wave orders in the presence of onsite interactions by performing FRG calculations. We find that interlayer repulsion suppresses the interlayer intra-orbital  $s_{\pm}$ -wave pairing and SDW order and drives a transition to an interlayer inter-orbital  $d_{x^2-y^2}$  pairing and a mirror-symmetry-breaking charge order. This transition occurs across a wide range of charge doping and is independent of the presence of the  $\gamma$  pocket. However, the critical scale of the  $d_{x^2-y^2}$ -wave superconductivity is significantly lower than that of the interlayer  $s_{\pm}$ -wave superconductivity, suggesting that this  $d_{x^2-y^2}$ -wave pairing is unlikely to account for the observed high- $T_c$  su-

perconductivity. Additionally, the intralayer nearest-neighbor repulsion promotes an in-plane CDW order with a vector of  $(\pi, \pi)$  by suppressing  $s_{\pm}$ -wave superconductivity and SDW order. Our results highlight intriguing influence of nonlocal Coulomb repulsion and the robustness of interlayer pairing associated with the bilayer structure and multi-orbital nature, advancing the understanding of the complex electronic correlations in LNO.

*Acknowledgments.* We acknowledge the supports by National Natural Science Foundation of China (Grant No. 12494594, No. 11920101005, No. 11888101, No. 12047503, No. 12322405, No. 12104450), the Ministry of Science and Technology (Grant No. 2022YFA1403901), and the New Cornerstone Investigator Program. X.W. is supported by the National Key R&D Program of China (Grant No. 2023YFA1407300) and the National Natural Science Foundation of China (Grant No. 12447103). C.C.L. is supported by the RIKEN TRIP initiative (RIKEN Quantum).

*Note added.* During the preparation of this work, we became aware of independent studies of interlayer interaction effects in  $\text{La}_3\text{Ni}_2\text{O}_7$  using RPA [58], DMRG [59] FLEX [60]. The conclusion of [60] that interlayer Coulomb interactions can drive a transition from  $s_{\pm}$  to  $d_{x^2-y^2}$ -wave pairing is consistent with our findings. In our work, we systematically explore the effects of nonlocal Coulomb repulsion, including both interlayer and intralayer interactions, on superconducting and density wave instabilities.

## Appendix A: FRG details

We implement our FRG calculations in the truncated unity functional renormalization group (TUFRG) formalism [56, 57]. In TUFRG, the static four point vertex function is decomposed into a scale independent initial bare interaction  $V^{(0)}$  plus three coupling functions  $\Phi^X$ ,  $X \in \{P, C, D\}$ ,

$$V^{\Lambda} = V^{(0)} + \Phi^P(\Lambda) + \Phi^C(\Lambda) + \Phi^D(\Lambda). \quad (\text{A1})$$

Here  $V^{(0)} \equiv V^{\Lambda_0}$  is the initial bare interaction, and  $\Phi^P$ ,  $\Phi^C$ , and  $\Phi^D$  are the single-channel coupling function in the particle-particle, crossed particle-hole, and direct particle-hole channels respectively. The static single channel coupling functions flow according to

$$\begin{aligned} \frac{d}{d\Lambda} \Phi_{\{o_i\}}^P(\mathbf{k}_1, \mathbf{k}_2; \mathbf{k}_3, \mathbf{k}_4) &= \mathcal{T}_{\{o_i\}}^{\text{pp}}(\mathbf{k}_1, \mathbf{k}_2; \mathbf{k}_3, \mathbf{k}_4) \\ \frac{d}{d\Lambda} \Phi_{\{o_i\}}^C(\mathbf{k}_1, \mathbf{k}_2; \mathbf{k}_3, \mathbf{k}_4) &= \mathcal{T}_{\{o_i\}}^{\text{cph}}(\mathbf{k}_1, \mathbf{k}_2; \mathbf{k}_3, \mathbf{k}_4) \\ \frac{d}{d\Lambda} \Phi_{\{o_i\}}^D(\mathbf{k}_1, \mathbf{k}_2; \mathbf{k}_3, \mathbf{k}_4) &= \mathcal{T}_{\{o_i\}}^{\text{dph}}(\mathbf{k}_1, \mathbf{k}_2; \mathbf{k}_3, \mathbf{k}_4) \end{aligned} \quad (\text{A2})$$

where  $\mathcal{T}_{\{o_i\}}^{\text{pp}}$ ,  $\mathcal{T}_{\{o_i\}}^{\text{cph}}$ ,  $\mathcal{T}_{\{o_i\}}^{\text{dph}}$  are contributions to the flow of interaction in particle-particle, direct particle-hole, crossed particle-hole channels respectively with Feynman diagrams shown in Fig. 9. For a general coupling function  $\mathcal{F}_{\{o_i\}}(\mathbf{k}_1, \mathbf{k}_2; \mathbf{k}_3, \mathbf{k}_4)$ , projections onto three channels P, C and D are defined as

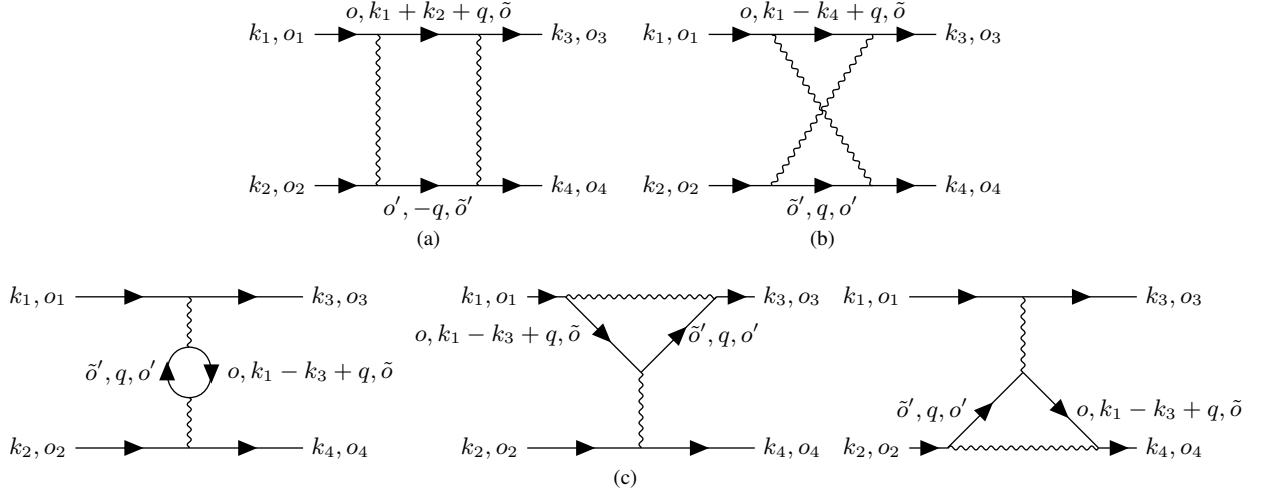


FIG. 9: One-loop contributions to the renormalization of interaction in orbit basis of multi-orbit system:(a)The particle-particle term. (b)The crossed particle-hole term. (c)The direct particle-hole terms.

$$\mathcal{F}^P = \hat{P}[\mathcal{F}], \quad \mathcal{F}^C = \hat{C}[\mathcal{F}], \quad \mathcal{F}^D = \hat{D}[\mathcal{F}],$$

$$\mathcal{F}_{o_1 o_2 m, o_3 o_4 n}^P(\mathbf{q}) = S_{\text{BZ}}^{-2} \int d\mathbf{k} d\mathbf{k}' f_m(\mathbf{k}) \mathcal{F}_{o_1 o_2 o_3 o_4}(\mathbf{k} + \mathbf{q}, -\mathbf{k}; \mathbf{k}' + \mathbf{q}, -\mathbf{k}') f_n^*(\mathbf{k}'), \quad (\text{A3})$$

$$\mathcal{F}_{o_1 o_4 m, o_3 o_2 n}^C(\mathbf{q}) = S_{\text{BZ}}^{-2} \int d\mathbf{k} d\mathbf{k}' f_m(\mathbf{k}) \mathcal{F}_{o_1 o_2 o_3 o_4}(\mathbf{k} + \mathbf{q}, \mathbf{k}'; \mathbf{k}' + \mathbf{q}, \mathbf{k}) f_n^*(\mathbf{k}'), \quad (\text{A4})$$

$$\mathcal{F}_{o_1 o_3 m, o_4 o_2 n}^D(\mathbf{q}) = S_{\text{BZ}}^{-2} \int d\mathbf{k} d\mathbf{k}' f_m(\mathbf{k}) \mathcal{F}_{o_1 o_2 o_3 o_4}(\mathbf{k} + \mathbf{q}, \mathbf{k}'; \mathbf{k}, \mathbf{k}' + \mathbf{q}) f_n^*(\mathbf{k}'). \quad (\text{A5})$$

Here  $f_m(\mathbf{k})$  are some formfactor basis satisfying orthogonality and completeness relations

$$S_{\text{BZ}}^{-1} \sum_m f_m(\mathbf{k}) f_m^*(\mathbf{k}') = \delta(\mathbf{k} - \mathbf{k}'), \quad S_{\text{BZ}}^{-1} \int d\mathbf{k} f_m(\mathbf{k}) f_n^*(\mathbf{k}) = \delta_{mn}. \quad (\text{A6})$$

The inverse transformations of above projections read

$$\begin{aligned} \mathcal{F}_{o_1 o_2 o_3 o_4}(\mathbf{k} + \mathbf{q}, -\mathbf{k}; \mathbf{k}' + \mathbf{q}, -\mathbf{k}') &= \sum_{mn} f_m^*(\mathbf{k}) \mathcal{F}_{o_1 o_2 m, o_3 o_4 n}^P(\mathbf{q}) f_n(\mathbf{k}'), \\ \mathcal{F}_{o_1 o_2 o_3 o_4}(\mathbf{k} + \mathbf{q}, \mathbf{k}'; \mathbf{k}' + \mathbf{q}, \mathbf{k}) &= \sum_{mn} f_m^*(\mathbf{k}) \mathcal{F}_{o_1 o_4 m, o_3 o_2 n}^C(\mathbf{q}) f_n(\mathbf{k}'), \\ \mathcal{F}_{o_1 o_2 o_3 o_4}(\mathbf{k} + \mathbf{q}, \mathbf{k}'; \mathbf{k}, \mathbf{k}' + \mathbf{q}) &= \sum_{mn} f_m^*(\mathbf{k}) \mathcal{F}_{o_1 o_3 m, o_4 o_2 n}^D(\mathbf{q}) f_n(\mathbf{k}'). \end{aligned} \quad (\text{A7})$$

In the singular mode-FRG (SMFRG) [57] or truncated unity-FRG (TUFGRG) [56] formalism, three bosonic propagators are defined by projecting single channel coupling functions onto three channels,

$$P = \hat{P}[\Phi^P], \quad C = \hat{C}[\Phi^C], \quad D = \hat{D}[\Phi^D]. \quad (\text{A8})$$

One also define  $V^{P,C,D}$  as projections of the effective interactions  $V^\Lambda$  onto three channels,

$$V^P = \hat{P}[V], \quad V^C = \hat{C}[V], \quad V^D = \hat{D}[V]. \quad (\text{A9})$$

The TUFGRG flow equations for the bosonic propagators read

$$\begin{aligned} \frac{d}{d\Lambda} P(\mathbf{q}) &= V^P(\mathbf{q}) \left[ \frac{d}{d\Lambda} \chi^{\text{pp}}(\mathbf{q}) \right] V^P(\mathbf{q}), \quad \frac{d}{d\Lambda} C(\mathbf{q}) = V^C(\mathbf{q}) \left[ \frac{d}{d\Lambda} \chi^{\text{ph}}(\mathbf{q}) \right] V^C(\mathbf{q}), \\ \frac{d}{d\Lambda} D(\mathbf{q}) &= [V^C(\mathbf{q}) - V^D(\mathbf{q})] \left[ \frac{d}{d\Lambda} \chi^{\text{ph}}(\mathbf{q}) \right] V^D(\mathbf{q}) + V^D(\mathbf{q}) \left[ \frac{d}{d\Lambda} \chi^{\text{ph}}(\mathbf{q}) \right] [V^C(\mathbf{q}) - V^D(\mathbf{q})]. \end{aligned} \quad (\text{A10})$$

Here  $\chi^{\text{pp/ph},\Lambda}$  is particle-particle/particle-hole susceptibility matrix in orbit and formfactor basis,

$$\begin{aligned}\chi_{oo'\bar{o}\bar{o}',mn}^{\text{pp}}(\mathbf{q}) &= - \int_{\mathbf{p}} f_m(\mathbf{p}) [G_{o\bar{o}}^\Lambda(i\omega, \mathbf{q} + \mathbf{p}) G_{o'\bar{o}'}^\Lambda(-i\omega, -\mathbf{p})] f_n^*(\mathbf{p}), \\ \chi_{oo'\bar{o}\bar{o}',mn}^{\text{ph}}(\mathbf{q}) &= - \int_{\mathbf{p}} f_m(\mathbf{p}) [G_{o\bar{o}}^\Lambda(i\omega, \mathbf{q} + \mathbf{p}) G_{\bar{o}'o'}^\Lambda(i\omega, \mathbf{p})] f_n^*(\mathbf{p}).\end{aligned}\quad (\text{A11})$$

Using Eqs. (A1), (A8) and (A9) the projections can be expressed by  $P, C$  and  $D$ ,

$$\begin{aligned}V^{\text{P}} &= \hat{\text{P}}[V] = \hat{\text{P}}[V^{(0)} + \hat{\text{P}}^{-1}[P] + \hat{\text{C}}^{-1}[C] + \hat{\text{D}}^{-1}[D]] = V^{\text{P},0} + P + V^{\text{P}\leftarrow\text{C}} + V^{\text{P}\leftarrow\text{D}}, \\ V^{\text{C}} &= \hat{\text{C}}[V] = \hat{\text{C}}[V^{(0)} + \hat{\text{P}}^{-1}[P] + \hat{\text{C}}^{-1}[C] + \hat{\text{D}}^{-1}[D]] = V^{\text{C},0} + V^{\text{C}\leftarrow\text{P}} + C + V^{\text{C}\leftarrow\text{D}}, \\ V^{\text{D}} &= \hat{\text{D}}[V] = \hat{\text{D}}[V^{(0)} + \hat{\text{P}}^{-1}[P] + \hat{\text{C}}^{-1}[C] + \hat{\text{D}}^{-1}[D]] = V^{\text{D},0} + V^{\text{D}\leftarrow\text{P}} + V^{\text{D}\leftarrow\text{C}} + D.\end{aligned}\quad (\text{A12})$$

Thus (A10) become closed differential equations for exchange propagators. We then solve above TUFGRG flow equations with a hard Matsubara frequency cutoff in bare propagator,  $G_{oo'}^\Lambda(k) = G_{oo'}\theta(|\omega| - \Lambda)$ . The the particle-particle(-) and particle-hole(+) bubbles are

$$\begin{aligned}\frac{d}{d\Lambda}\chi_{\pm}^\Lambda(\mathbf{k}_1, \mathbf{k}_2) &= \frac{1}{2\pi}[(G(i\Lambda, \mathbf{k}_1)G(\pm i\Lambda, \mathbf{k}_2) \\ &\quad + G(-i\Lambda, \mathbf{k}_1)G(\mp i\Lambda, \mathbf{k}_2)]\end{aligned}\quad (\text{A13})$$

where orbit indexes are not written explicitly. The form factor basis is truncated to 9 terms, encompassing on-site, first-nearest-neighbor, and second-nearest-neighbor bonds.

The effective interactions in pairing, magnetic and charge channels are  $-V^{\text{P}}, V^{\text{C}}, V^{\text{C}} - 2V^{\text{D}}$  respectively. By diagonalizing the interaction matrices in different channels, expressed as  $V^{\text{ch}} = \sum_i \Xi_i^{\text{ch}} O_i^{\text{ch}} O_i^{\text{ch}\star}$ , the eigenmode  $O_i^{\text{ch}}$  with a positive eigenvalue  $\Xi_i^{\text{ch}}$  corresponds to an attractive channel. The channel with the most divergent eigenvalue  $\Xi$  is identified as the leading instability of the system. By diagonalizing the effective interaction matrices in real space orbit basis, the eigenmode with largest eigenvalue is identified as the leading instability.

## Appendix B: Effect of interlayer-interorbital repulsion

The effect of interlayer interorbital repulsion is illustrated in Fig. 10, where we include both interlayer intraorbital repulsion  $V_{\perp}^{zz} = 2V_{\perp}^{xx} = V_{\perp}$  and interorbital repulsion  $V_{\perp}^{xz}$ . The interlayer intraorbital effective pairing interaction

can further emerges from enhanced charge fluctuations and are generated from bubble diagram through  $V_{\perp}^{xz} - V_{\perp}^{zz}$  and  $V_{\perp}^{xz} - U'$  process. Moreover, The inclusion of interlayer interorbital repulsion suppresses interlayer  $d_{x^2-y^2}$  pairing. These enhances the robustness of  $s_{\pm}^{\text{I}}$  pairing, as shown in the phase diagram.

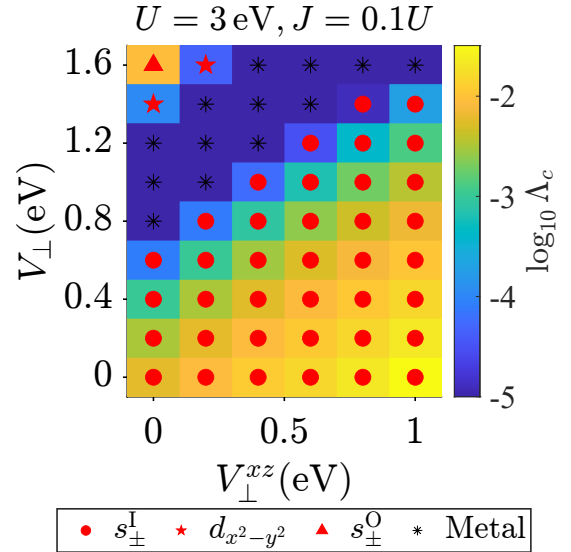


FIG. 10: (color online) interlayer-interorbital repulsion  $V_{\perp}^{xz}$  versus interlayer-intraorbital repulsion  $V_{\perp}$  phase diagram with  $U = 3 \text{ eV}$ ,  $J = 0.1U$ ,  $n = 3$ .

- [1] D. J. Scalapino, *Rev. Mod. Phys.* **84**, 1383 (2012).
- [2] P. A. Lee, N. Nagaosa, and X.-G. Wen, *Rev. Mod. Phys.* **78**, 17 (2006).
- [3] P. J. Hirschfeld, M. M. Korshunov, and I. I. Mazin, *Reports on Progress in Physics* **74**, 124508 (2011).
- [4] H. Sun, M. Huo, X. Hu, J. Li, Z. Liu, Y. Han, L. Tang, Z. Mao,

- P. Yang, B. Wang, J. Cheng, D.-X. Yao, G.-M. Zhang, and M. Wang, *Nature* **621**, 493 (2023).
- [5] Z. Luo, X. Hu, M. Wang, W. Wú, and D.-X. Yao, *Phys. Rev. Lett.* **131**, 126001 (2023).
- [6] Y. Zhang, L.-F. Lin, A. Moreo, and E. Dagotto, *Phys. Rev. B* **108**, L180510 (2023).

- [7] F. Lechermann, J. Gondolf, S. Bötzel, and I. M. Eremin, *Phys. Rev. B* **108**, L201121 (2023).
- [8] H. Sakakibara, N. Kitamine, M. Ochi, and K. Kuroki, *Phys. Rev. Lett.* **132**, 106002 (2024).
- [9] Y. Gu, C. Le, Z. Yang, X. Wu, and J. Hu, (2023), [arXiv:2306.07275](https://arxiv.org/abs/2306.07275).
- [10] J. Yang, H. Sun, X. Hu, Y. Xie, T. Miao, H. Luo, H. Chen, B. Liang, W. Zhu, G. Qu, C.-Q. Chen, M. Huo, Y. Huang, S. Zhang, F. Zhang, F. Yang, Z. Wang, Q. Peng, H. Mao, G. Liu, Z. Xu, T. Qian, D.-X. Yao, M. Wang, L. Zhao, and X. J. Zhou, (2023), [arXiv:2309.01148](https://arxiv.org/abs/2309.01148).
- [11] Z. Liu, M. Huo, J. Li, Q. Li, Y. Liu, Y. Dai, X. Zhou, J. Hao, Y. Lu, M. Wang, and H.-H. Wen, (2024), [arXiv:2307.02950](https://arxiv.org/abs/2307.02950).
- [12] Z. Liu, H. Sun, M. Huo, X. Ma, Y. Ji, E. Yi, L. Li, H. Liu, J. Yu, Z. Zhang, Z. Chen, F. Liang, H. Dong, H. Guo, D. Zhong, B. Shen, S. Li, and M. Wang, *Science China Physics, Mechanics & Astronomy* **66**, 217411 (2022).
- [13] K. Chen, X. Liu, J. Jiao, M. Zou, C. Jiang, X. Li, Y. Luo, Q. Wu, N. Zhang, Y. Guo, and L. Shu, *Phys. Rev. Lett.* **132**, 256503 (2024).
- [14] X. Chen, J. Choi, Z. Jiang, J. Mei, K. Jiang, J. Li, S. Agrestini, M. Garcia-Fernandez, H. Sun, X. Huang, D. Shen, M. Wang, J. Hu, Y. Lu, K.-J. Zhou, and D. Feng, *Nature Communications* **15**, 9597 (2024).
- [15] M. Kakoi, T. Oi, Y. Ohshita, M. Yashima, K. Kuroki, T. Kato, H. Takahashi, S. Ishiwata, Y. Adachi, N. Hatada, T. Uda, and H. Mukuda, *Journal of the Physical Society of Japan* **93**, 053702 (2024).
- [16] I. Plokhikh, T. J. Hicken, L. Keller, V. Pomjakushin, S. H. Moody, P. Foury-Leylekian, J. J. Krieger, H. Luetkens, Z. Guguchia, R. Khasanov, and D. J. Gawryluk, (2025), [arXiv:2503.05287](https://arxiv.org/abs/2503.05287).
- [17] M. Yashima, N. Seto, Y. Oshita, M. Kakoi, H. Sakurai, Y. Takano, and H. Mukuda, (2025), [arXiv:2503.09288](https://arxiv.org/abs/2503.09288).
- [18] R. Khasanov, T. J. Hicken, D. J. Gawryluk, V. Sazgari, I. Plokhikh, L. P. Sorel, M. Bartkowiak, S. Bötzel, F. Lechermann, I. M. Eremin, H. Luetkens, and Z. Guguchia, *Nature Physics* **21**, 430 (2025).
- [19] D. Zhao, Y. Zhou, M. Huo, Y. Wang, L. Nie, Y. Yang, J. Ying, M. Wang, T. Wu, and X. Chen, *Science Bulletin* (2025), <https://doi.org/10.1016/j.scib.2025.02.019>.
- [20] X. Ren, R. Sutarto, X. Wu, J. Zhang, H. Huang, T. Xiang, J. Hu, R. Comin, X. Zhou, and Z. Zhu, *Communications Physics* **8**, 52 (2025).
- [21] H. Sakakibara, M. Ochi, H. Nagata, Y. Ueki, H. Sakurai, R. Matsumoto, K. Terashima, K. Hirose, H. Ohta, M. Kato, Y. Takano, and K. Kuroki, (2024), [arXiv:2309.09462](https://arxiv.org/abs/2309.09462).
- [22] Q. Li, Y.-J. Zhang, Z.-N. Xiang, Y. Zhang, X. Zhu, and H.-H. Wen, *Chinese Physics Letters* **41**, 017401 (2024).
- [23] Y. Zhu, E. Zhang, B. Pan, X. Chen, D. Peng, L. Chen, H. Ren, F. Liu, N. Li, Z. Xing, J. Han, J. Wang, D. Jia, H. Wo, Y. Gu, Y. Gu, L. Ji, W. Wang, H. Gou, Y. Shen, T. Ying, X. Chen, W. Yang, C. Zheng, Q. Zeng, J. gang Guo, and J. Zhao, (2024), [arXiv:2311.07353](https://arxiv.org/abs/2311.07353).
- [24] M. Zhang, C. Pei, X. Du, W. Hu, Y. Cao, Q. Wang, J. Wu, Y. Li, H. Liu, C. Wen, Y. Zhao, C. Li, W. Cao, S. Zhu, Q. Zhang, N. Yu, P. Cheng, L. Zhang, Z. Li, J. Zhao, Y. Chen, H. Guo, C. Wu, F. Yang, S. Yan, L. Yang, and Y. Qi, (2024), [arXiv:2311.07423](https://arxiv.org/abs/2311.07423).
- [25] J. Li, C. Chen, C. Huang, Y. Han, M. Huo, X. Huang, P. Ma, Z. Qiu, J. Chen, X. Hu, *et al.*, *Sci. China Phys. Mech. Astron* **10** (2024).
- [26] E. K. Ko, Y. Yu, Y. Liu, L. Bhatt, J. Li, V. Thampy, C.-T. Kuo, B. Y. Wang, Y. Lee, K. Lee, J.-S. Lee, B. H. Goodge, D. A. Muller, and H. Y. Hwang, *Nature* **638**, 935 (2025).
- [27] G. Zhou, W. Lv, H. Wang, Z. Nie, Y. Chen, Y. Li, H. Huang, W. Chen, Y. Sun, Q.-K. Xue, and Z. Chen, *Nature* (2025), [10.1038/s41586-025-08755-z](https://doi.org/10.1038/s41586-025-08755-z).
- [28] M. Shi, D. Peng, Y. Li, Z. Xing, Y. Wang, K. Fan, H. Li, R. Wu, Z. Zeng, Q. Zeng, J. Ying, T. Wu, and X. Chen, (2025), [arXiv:2501.14202](https://arxiv.org/abs/2501.14202).
- [29] Q.-G. Yang, D. Wang, and Q.-H. Wang, *Phys. Rev. B* **108**, L140505 (2023).
- [30] C. Lu, Z. Pan, F. Yang, and C. Wu, *Phys. Rev. Lett.* **132**, 146002 (2024).
- [31] H. Oh and Y.-H. Zhang, *Phys. Rev. B* **108**, 174511 (2023).
- [32] J. Zhan, Y. Gu, X. Wu, and J. Hu, (2024), [arXiv:2404.03638](https://arxiv.org/abs/2404.03638).
- [33] Y.-B. Liu, J.-W. Mei, F. Ye, W.-Q. Chen, and F. Yang, *Phys. Rev. Lett.* **131**, 236002 (2023).
- [34] X.-Z. Qu, D.-W. Qu, J. Chen, C. Wu, F. Yang, W. Li, and G. Su, *Phys. Rev. Lett.* **132**, 036502 (2024).
- [35] Y.-f. Yang, G.-M. Zhang, and F.-C. Zhang, *Phys. Rev. B* **108**, L201108 (2023).
- [36] Q. Qin and Y.-f. Yang, *Phys. Rev. B* **108**, L140504 (2023).
- [37] D.-C. Lu, M. Li, Z.-Y. Zeng, W. Hou, J. Wang, F. Yang, and Y.-Z. You, (2023), [arXiv:2308.11195](https://arxiv.org/abs/2308.11195).
- [38] Y.-H. Tian, Y. Chen, J.-M. Wang, R.-Q. He, and Z.-Y. Lu, (2023), [arXiv:2308.09698](https://arxiv.org/abs/2308.09698).
- [39] Y. Zhang, L.-F. Lin, A. Moreo, T. A. Maier, and E. Dagotto, *Phys. Rev. B* **108**, 165141 (2023).
- [40] Y. Zhang, L.-F. Lin, A. Moreo, T. A. Maier, and E. Dagotto, *Nature Communications* **15**, 2470 (2024).
- [41] K. Jiang, Z. Wang, and F.-C. Zhang, *Chinese Physics Letters* **41**, 017402 (2024).
- [42] F. Lechermann, J. Gondolf, S. Bötzel, and I. M. Eremin, *Phys. Rev. B* **108**, L201121 (2023).
- [43] Z. Liao, L. Chen, G. Duan, Y. Wang, C. Liu, R. Yu, and Q. Si, *Phys. Rev. B* **108**, 214522 (2023).
- [44] S. Ryee, N. Witt, and T. O. Wehling, *Phys. Rev. Lett.* **133**, 096002 (2024).
- [45] Z. Luo, B. Lv, M. Wang, W. Wú, and D.-X. Yao, *npj Quantum Materials* **9**, 61 (2024).
- [46] Z. Fan, J.-F. Zhang, B. Zhan, D. Lv, X.-Y. Jiang, B. Normand, and T. Xiang, *Phys. Rev. B* **110**, 024514 (2024).
- [47] R. Jiang, J. Hou, Z. Fan, Z.-J. Lang, and W. Ku, *Phys. Rev. Lett.* **132**, 126503 (2024).
- [48] K. Jiang, Z. Wang, and F.-C. Zhang, *Chinese Physics Letters* **41**, 017402 (2024).
- [49] H. Schlömer, U. Schollwöck, F. Grusdt, and A. Bohrdt, *Communications Physics* **7**, 366 (2024).
- [50] V. Christiansson, F. Petocchi, and P. Werner, *Phys. Rev. Lett.* **131**, 206501 (2023).
- [51] C. Le, J. Zhan, X. Wu, and J. Hu, (2025), [arXiv:2501.14665](https://arxiv.org/abs/2501.14665).
- [52] C. Castellani, C. R. Natoli, and J. Ranninger, *Phys. Rev. B* **18**, 4945 (1978).
- [53] M. Salmhofer and C. Honerkamp, *Progress of Theoretical Physics* **105**, 1 (2001).
- [54] W. Metzner, M. Salmhofer, C. Honerkamp, V. Meden, and K. Schönhammer, *Rev. Mod. Phys.* **84**, 299 (2012).
- [55] C. Platt, W. Hanke, and R. Thomale, *Advances in Physics* **62**, 453 (2013).
- [56] J. Lichtenstein, D. Sánchez de la Peña, D. Rohe, E. Di Napoli, C. Honerkamp, and S. A. Maier, *Computer Physics Communications* **213**, 100 (2017).
- [57] W.-S. Wang, Y.-Y. Xiang, Q.-H. Wang, F. Wang, F. Yang, and D.-H. Lee, *Phys. Rev. B* **85**, 035414 (2012).
- [58] L. B. Braz, G. B. Martins, and L. G. G. V. D. da Silva, (2025), [arXiv:2502.08425](https://arxiv.org/abs/2502.08425).

[59] P. Borchia, H. Lange, and F. Grusdt, (2025), [arXiv:2502.13960](#)

[60] W. Xi, S.-L. Yu, and J.-X. Li, [Phys. Rev. B \*\*111\*\*, 104505 \(2025\)](#).